

Physics-Based Model for Nonuniform Thermionic Electron Emission from Polycrystalline Cathodes

Dongzheng Chen^{1,*}, Ryan Jacobs,¹ John Petillo², Vasilios Vlahos,³ Kevin L. Jensen⁴,
Dane Morgan,¹ and John Booske⁵


¹Department of Materials Science and Engineering, University of Wisconsin-Madison, 1509 University Ave,
Madison, Wisconsin 53706, USA

²Leidos, 700 Technology Park Dr., Billerica, Massachusetts 01821, USA

³Viasat Space Systems, 2040 E. Technology Circle, Tempe, Arizona 85284, USA

⁴Code 6362, MSTD, Naval Research Laboratory, Washington, DC 20375, USA

⁵Department of Electrical and Computer Engineering, University of Wisconsin-Madison, 1415 Engineering Dr.,
Madison, Wisconsin 53706, USA

 (Received 14 December 2021; revised 6 August 2022; accepted 9 September 2022; published 3 November 2022)

A physics-based model that predicts the emitted current from thermionic cathodes is developed, which accurately spans from the temperature-limited (TL) to full-space-charge-limited (FSCL) regions. Experimental observations of thermionic electron emission demonstrate a smooth transition between TL and FSCL regions of the emitted-current-density-versus-temperature (J - T) (Miram) curve and the emitted-current-density-versus-voltage (J - V) curve. Knowledge of the temperature and shape of the TL-FSCL transition is important in evaluating the thermionic electron-emission performance of cathodes, including predicting the lifetime. However, there are no first-principles physics-based models that predict the smooth TL-FSCL transition region for real thermionic cathodes without applying *a priori* assumptions or empirical phenomenological equations that are physically difficult to justify. Previous work detailing the nonuniform thermionic emission found that the effects of three-dimensional space charge, patch fields (electrostatic potential nonuniformity on the cathode surface based on local work-function values), and Schottky barrier lowering can lead to a smooth TL-FSCL transition region from a model thermionic cathode surface with a checkerboard spatial distribution of work-function values. In this work, we construct a physics-based nonuniform emission model for commercial dispenser cathodes. This emission model is obtained by incorporating the cathode surface grain orientation via electron-backscatter diffraction and the facet-orientation-specific work-function values from density-functional-theory calculations. The model enables the construction of two-dimensional emitted-current-density maps of the cathode surface and corresponding J - T and J - V curves. The predicted emission curves show excellent agreement with experiment, not only in the TL and FSCL regions but, crucially, also in the TL-FSCL transition region. This model provides a method to predict the thermionic emission from the microstructure of a commercial cathode and improves the understanding of the relationship between thermionic emission and cathode microstructure, which is beneficial for the design of vacuum electronic devices.

DOI: [10.1103/PhysRevApplied.18.054010](https://doi.org/10.1103/PhysRevApplied.18.054010)

I. INTRODUCTION

Thermionic electron-emission cathodes based on porous, polycrystalline W combined with mixtures of metal oxides (typically BaO-CaO-Al₂O₃) mark a significant evolutionary step in the history of thermionic cathodes, as these dispenser cathodes produce high-current-density emission with long lifetimes due to their dynamically stable low-work-function surfaces [1]. There are some widely used mixture ratios for the metal oxides

in the dispenser cathodes. The most common mix is BaO : CaO:Al₂O₃ = 5:3:2 (a *B*-type cathode), which produces emitted current densities of several A/cm². There are other variations, including the 4:1:1 cathode (*S*-type), which is resistant to surface poisoning and can usually be operated at a temperature 30 °C lower than other types [2–5]. More recent dispenser cathodes include the *M*-type and scandate cathodes, which have a lower effective work function than the *B*- and *S*-type cathodes [6–8]. The *B*-, *S*-, and *M*-type cathodes have constituted the majority of commercial thermionic cathodes for the past 50 years and are used as the electron sources in numerous vacuum

*dchen255@wisc.edu

electronic devices, such as communication devices, ion thrusters, thermionic energy converters, and free-electron lasers. These applications, taken together, influence multiple facets of our modern life, ranging from defense, satellite communications, radar, and scientific research to industrial-scale food production and the manufacture of heat-harvesting renewable-energy technology [9,10].

Numerous experimental and computational studies show that the microstructure of real W-based cathodes is complex. The tungsten bodies are polycrystalline and porous, and the cathode surfaces are spatially heterogeneous, with the presence of machining marks from the cathode-manufacturing process also contributing to the heterogeneity and local field-enhancement effects [4, 11–13]. One of the results of the complex microstructure is that W-based cathodes are spatially heterogeneous with a distribution of grain sizes and many types of exposed surfaces. These surfaces might have varied crystal facets and metal oxide coatings, each with an associated work-function value, leading to highly nonuniform emission [3,5,6,8,14–17]. The nonuniform nature of thermionic electron emission from polycrystalline W is observed experimentally by using thermionic electron-emission microscopy (ThEEM) [16,18–27]. In a representative ThEEM image, at a particular temperature, certain grains of the W surface are bright while others remain dark, indicating that some grains are more emissive than others, due to factors such as lower work function and surface topography.

Emitted-current-density-versus-temperature, or J - T (Miram), curves and emitted-current-density-versus-voltage, or J - V (I - V), curves are commonly used to evaluate the cathode performance. Both the J - T and J - V curves of a cathode can be divided into three regions: the temperature-limited (TL) region, the full-space-charge-limited (FSCL) region, and the TL-FSCL transition region. The TL region is in the low-temperature end of a J - T curve or the high-voltage end of a J - V curve. Its behavior can be well described with the Richardson-Laue-Dushman equation [28,29] with Schottky-barrier lowering [30]. The FSCL region is in the high-temperature end of a J - T curve or the low-voltage end of a J - V curve. The behavior can be predicted by the Child-Langmuir law [31,32] and Langmuir and Fry’s models [32,33], including provision for two-dimensional edge-correction effects [34–40]. Experimental observations on real thermionic cathodes show that the TL-FSCL region is usually smooth, sometimes referred to as the “roll-off.” Despite this seemingly simple observed behavior, it remains an ongoing challenge to develop a physics-based emission model that is able to accurately predict the behavior of both J - T and J - V curves from polycrystalline cathodes over the entire operational domain of temperature and anode-cathode voltage, and especially challenging to capture the smooth transition between the TL and FSCL regions for real

cathodes. Thermionic cathodes are typically operated on the FSCL side near the TL-FSCL transition region, so that the changes in cathode temperature over time do not cause large variations in the emitted current and that the emission is stable over the predicted lifetime of the device.

Some empirical descriptions of the smooth TL-FSCL region have been developed, including the empirical Longo-Vaughan equation [41,42], a continuous Gaussian distribution of work function [43], the work-function distribution mathematical treatment of emission data [44], and the practical work-function distribution [45]. However, all of these models are based on empirical equations or *a priori* assumptions that are difficult to justify, such as the assumption that different work-function patches do not interact. Furthermore, these empirical descriptions are not able to reveal the fundamental origin of the smooth behavior of the TL-FSCL transition, thus limiting their usefulness for modeling cathode behavior under different operating conditions.

A number of previous works have studied the interplay of a heterogeneous cathode surface on the resulting thermionic emission and have sought to connect the smooth TL-FSCL transition to the spatial distribution of work-function values. The theory of the anomalous Schottky effect [46] studies the contribution of the patch field effect (electrostatic potential nonuniformity on the cathode surface based on local work-function values) and the Schottky-barrier-lowering effect on the smoothness of the TL-FSCL transition in J - V curves. Studies on space-charge effects [39,40,47,48] reveal the contribution of three-dimensional (3D) space-charge fields on the smooth transition in J - T curves. However, the TL-FSCL transition behaviors predicted from these two separate sets of studies are sharper than experimental observations, indicating that some physical effects are missing. There has been no physics-based emission model that can predict the TL-FSCL transition in agreement with experimental results, although Longo [41] and Vaughan speculated [42] that sharper Miram curve knees might be associated with more uniform work-function surfaces or “better” cathodes. Our recent work [49] developed a physics-based model that included the effects of nonuniform thermionic emission, 3D space charge, patch fields, and Schottky-barrier lowering. That work gave a mathematical method to calculate the emitted current from a cathode with a spatially heterogeneous work-function distribution in an infinite parallel diode, and it was able to predict a smooth and gradual TL-FSCL transition comparable with experimental observations by using a checkerboard work-function distribution. Those findings are encouraging and indicate that our model may be able to predict the emission of a real cathode, including the smooth TL-FSCL transition, by applying a two-dimensional work-function map obtained from the same real cathode.

Here, we construct a two-dimensional work-function map by incorporating the grain orientation via electron-backscatter diffraction (EBSD) and the facet-orientation-specific work-function values from density-functional-theory (DFT) calculations. We use this work-function map in conjunction with the nonuniform emission model developed in our previous work [49] to predict both the J - T (Miram) and J - V (I - V) curves, including the TL-FSCL transition. Overall, we find semiquantitative agreement of our predicted results with experimental measurements. In this work, a physics-based thermionic emission model incorporating heterogeneous surface effects from a work-function distribution on a real commercial thermionic cathode is used to successfully model the experimental emission over a wide domain of temperature and applied voltage and illustrates that accurate modeling of the J - T (Miram) and J - V (I - V) characteristics of a real polycrystalline cathode is practical. Moreover, this work establishes that an experimentally derived nonuniform work-function distribution is able to self-consistently and quantitatively predict the J - T and J - V characteristics of a real polycrystalline cathode over a very wide range of parameter values, without the need for significant adjustment of any empirical fitting factors.

II. METHODS

A. Cathode sample

The cathode analyzed in this work is a commercial S -type cathode made by 3M Technical Ceramics. The cathode is made of 80% density W using standard manufacturing methods and impregnated with an oxide mixture of $\text{BaO}:\text{CaO}:\text{Al}_2\text{O}_3 = 4:1:1$. The cathode is cylinder shaped with a diameter of 2.77 mm and height of 0.97 mm, as measured after the emission test. The cathode body is cylindrical in shape, and the surface of the cathode is macroscopically flat.

B. Emission measurement

The experimental results of emitted current are measured in a closely spaced diode-testing vehicle (Fig. 1). The heater and anode fixtures are manufactured by L3-Harris. The anode-cathode distance in this setup for a 0.97-mm-high cathode is designed to be $d = 1.06$ mm. A molybdenum ring is placed around the cathode to shield side emission from the sides. The height of the molybdenum ring is 1.14 mm, which is 0.17 mm higher than the cathode. The inner diameter of 2.90 mm is 0.13 mm larger than the diameter of the cathode. The heater filament is powered by a Keithley 2200-20-5 programmable power supply, which is operated in constant-current mode.

To make it possible to measure the temperature of the cathode surfaces using a pyrometer during operation, a triode design is used with a hollow cylinder as the current

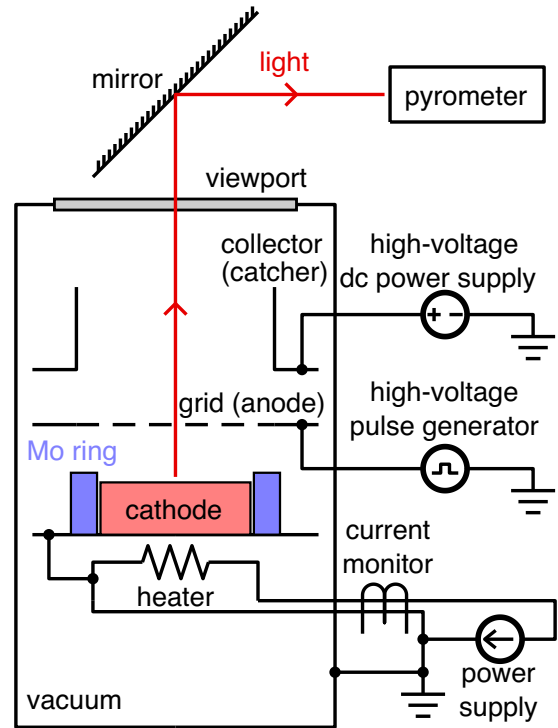


FIG. 1. Sketch of the closely spaced diode-testing vehicle used to measure the thermionic emitted current. Rectangle filled with pink is the cathode. Purple rectangles around the cathode represent the molybdenum ring used to shield side emission.

collector or “catcher.” The temperature of the cathode surface is measured with an optical pyrometer made by Leeds & Northrup Co. (Catalogue No. 8622), which is a $\lambda = 0.65$ - μm single-wavelength disappearing-filament pyrometer. The electron-emission-cathode industry often simply uses the pyrometer reading to indicate the cathode temperature, reporting it as the brightness temperature. However, the true temperature of the cathode surface is needed to use our nonuniform emission model [49]. We calibrate the temperature values using Planck’s law. The radiation of the cathode received by the disappearing pyrometer at wavelength λ is

$$tr\epsilon \frac{2hc^2}{\lambda^5} \frac{1}{e^{hc/(\lambda kT)} - 1} = \frac{2hc^2}{\lambda^5} \frac{1}{e^{hc/(\lambda kT_b)} - 1}, \quad (1)$$

where T_b is the pyrometer reading (brightness temperature), T is the calibrated “true” temperature of the cathode surface to be used in the emission model, k is the Boltzmann constant, h is the Planck constant, and c is the speed of light. The values of the transmissivity of the viewport, $t = 0.93$, and the reflectivity of the mirror, $r = 0.76$, in the optical path are as measured. In this study, we use an emissivity value of $\epsilon = 0.52$, which is recommended for impregnated W cathodes [2]. The uncertainty of the measured temperature values is approximately ± 20 °C.

The cathode is activated before the emission tests, following instructions from the cathode manufacturer, 3M Technical Ceramics. The activation process includes four steps: (1) slowly increase the cathode temperature to a brightness temperature of 1000 °C, and then hold this temperature for 30 min; (2) continue to increase the cathode temperature to a brightness temperature of 1175–1200 °C and hold for 1 h; (3) cool the cathode to a brightness temperature of 1100–1150 °C and hold for 2 h; and (4) reduce the cathode temperature and measure the emitted current while cooling the cathode. The pressure is kept below 5×10^{-6} torr during the activation process.

During the emission measurements, the grid is biased with a PVX-4110 high-voltage pulse generator made by Directed Energy (DEI), which is powered by a dc high-voltage power supply made by Glassman High Voltage, Inc. (Model No. PS/ER02R150-115), and controlled by a low-voltage pulse generator, Model 575 pulse and delay generator made by Berkeley Nucleonics Corp (BNC). The catcher is biased with a dc high-voltage power supply made by Glassman High Voltage, Inc. (Model No. PS/EQ005R240-22) and is kept more positively biased than the grid. The voltages of the grid and the catcher are measured with a LeCroy 44Xs oscilloscope. The emitted current is measured with the same oscilloscope via a Model 4100C current monitor made by Pearson Electronics, Inc.

C. Microstructure characterization

The cathode surface-grain orientation is characterized using EBSD in an FEI Helios G4 Plasma FIB-FESEM-EBSD-EDS workstation after the emission test. The surface of commercial dispenser cathodes is usually rough due to the machining process of cutting the cathode pellets on a lathe. Machining typically produces micrometer-scale ridges, and those differences can be seen in the variation in emission properties [50]. Confidence-index (CI) values in the EBSD results are used to quantify the likelihood of correct grain-orientation labeling [51]. CI standardization, one of the built-in cleanup algorithms in OIM Analysis™ by EDAX, software for EBSD analysis, is used to process raw EBSD data. Pixels with low CI values after applying the CI standardization cleanup procedure are considered as areas where grain orientations are unable to be correctly labeled by EBSD [52], and the surface-facet orientation cannot be reliably determined. Visual inspection shows that the majority of pixels with a CI lower than 0.1 are associated with nonemitting areas, such as rough valleys, depressions, grain boundaries, and pores [53]. Thus, areas with CI less than 0.1 are considered as no-emit areas, and the grain orientation of areas with CI greater than or equal to 0.1 are considered as recognizable areas. We then use simulations described below to establish a two-dimensional work-function map, $\phi_{\text{DFT}}(x, y)$, for areas with CI greater than or equal to 0.1.

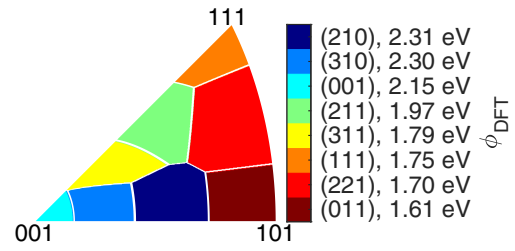


FIG. 2. Inverse polar figure (IPF) showing how a grain orientation is grouped into one of the eight orientation groups using the nearest-neighbor algorithm. Colors indicate the work-function values assigned to each orientation group, which are the work-function values of the W surface with most stable stoichiometric Ba-O adsorption calculated by DFT.

D. Density-functional-theory work-function values

Previous DFT studies calculated the work functions and surface stabilities of tungsten surfaces with Ba, O, and Ba-O adsorbates of eight different orientations: (001), (011), (111), (210), (211), (221), (310), (311) [5,6,17]. Auger analysis indicates that the active state for impregnated cathodes can be reproduced by a near monolayer of stoichiometric Ba-O on the W surface [15]. Only the DFT work-function value for the most stable stoichiometric Ba-O adsorption is used to assign to each orientation (Table I). For a high-index orientation (hkl) other than the calculated eight orientations, the nearest-neighbor algorithm is used to predict its work function [54]. It is assumed that a facet with an (hkl) orientation had the same work function as the one among the calculated eight orientations with the smallest misorientation with (hkl) (Fig. 2).

A few studies estimate the uncertainty of DFT work-function values by comparing DFT results with experimental results. De Waele *et al.* [55] compared the experimental work-function values for different surface orientations for a number of metals with the values predicted by

TABLE I. List of eight orientations with work-function values predicted using DFT. ϕ_{DFT} is the DFT work-function value for the most stable stoichiometric Ba-O adsorption for each orientation. $\phi_{\text{DFT}} + \Delta\phi$ is the shifted work-function value, where the shift is $\Delta\phi = 0.176$ eV. The “percentage” column shows the percentage of each orientation group in Fig. 3.

Orientation	ϕ_{DFT} (eV)	$\phi_{\text{DFT}} + \Delta\phi$ (eV)	Percentage (%)
(001)	2.15	2.326	6.3
(011)	1.61	1.786	5.5
(111)	1.75	1.926	2.3
(210)	2.31	2.486	8.9
(211)	1.97	2.146	14.0
(221)	1.70	1.876	12.7
(310)	2.30	2.476	19.3
(311)	1.79	1.966	13.8
Unrecognized			17.1

the Perdew-Burke-Ernzerhof (PBE) parametrization of the generalized-gradient-approximation (GGA) method. They perform a linear fit of DFT values, ϕ_{DFT} , and experimental values, $\phi_{\text{expt.}}$. The result is the equation $\phi_{\text{expt.}} = \beta_1 \phi_{\text{DFT}} + \beta_0$, where the values of the fitted coefficients are $\beta_1 = (0.99 \pm 0.02)\text{eV}$ and $\beta_0 = (0.30 \pm 0.09)\text{eV}$. Tran *et al.* [56] also compared their DFT results, ϕ_{DFT} , with experimental values, $\phi_{\text{expt.}}$, on single crystals. They make a single-parameter $\phi_{\text{DFT}} = \phi_{\text{expt.}} - c$ least-squares fit, where their result is $c = 0.30\text{eV}$. Both results indicate that DFT work-function predictions of metals using GGA-level functionals tend to underestimate the work-function values by approximately 0.30 eV, on average, compared with experimental results and that the error of the estimate is on the scale of tenths of eV even after the linear fit. Due to this known underestimation, we consider the shift between experimental and calculated work function as a fitting parameter in our emission modeling (more details are given in Sec. II E).

E. Emission modeling

It is prohibitively difficult to accurately measure, and thus, to know, the exact anode-cathode distance, d , at the operating temperatures in our test fixture. Therefore, to better compare the results of the emission model with the experimental results, in this work, we obtain the effective anode-cathode distance, d , by fitting FSCL data points with the Child-Langmuir law with the finite-temperature correction in an infinite parallel diode [32]:

$$J_{\text{FSCL}} = \frac{4\epsilon_0}{9} \sqrt{\frac{2e}{m}} \frac{(V - V_m)^{3/2}}{(d - z_m)^2} \frac{9}{8\sqrt{\pi}} \eta^{-3/2} \times \left(\int_0^\eta \frac{d\eta}{\sqrt{\text{erfcx}\sqrt{\eta} - 1 + 2\sqrt{\eta/\pi}}} \right)^2, \quad (2)$$

where ϵ_0 is the vacuum permittivity; e is the elementary charge; m is the electron mass; V is the anode-cathode voltage; d is the anode-cathode distance; V_m and z_m are the voltage and location from the cathode of the voltage minimum, respectively; $\eta = e(V - V_m)/(kT)$, where k is the Boltzmann constant and T is the temperature; and erfcx is the scaled complementary error function. Instead of using the as-designed value of the anode-cathode distance, we use the fitted value for the emission model, which we believe is a more accurate value for high temperatures during emission measurements. Based on our experience and that of others, the use of a cathode-diameter-to-gap-ratio of approximately three, and the use of the molybdenum edge-emission suppression ring are sufficient to enable using the infinite-area form of Eq. (2) to estimate the anode-cathode gap at high temperature.

In the theory of the Child-Langmuir law with the finite-temperature correction on a uniform cathode [32], the

voltage minimum satisfies the Richardson-Laue-Dushman equation, $J = AT^2 \exp[-eV_m/(kT)]$, while the voltage-minimum position, $z_m = 0$, at the TL-FSCL transition. When fitting d using Eq. (2), we make the same assumptions, $z_m = 0$ and $J = AT^2 \exp[-eV_m/(kT)]$, where J is the experimentally measured emitted current density. Here, $A = 4\pi me k^2/h^3 = 120.173\text{A}/\text{cm}^{-2}\text{K}^{-2}$ is the Richardson constant, where h is Planck's constant.

It is not practical to do EBSD on the whole surface of a cathode, so we characterize the grain orientation on a representative area of the cathode surface (more details are given in Sec. III D) and use periodic boundary conditions on the edges of the work-function map, considering that the nonuniform emission model [49] is designed for spatially periodic work-function maps. Considering the error in the DFT work-function values, we add a constant shift, $\Delta\phi$, to the DFT work-function values, $\phi_{\text{DFT}}(x, y)$, to get a shifted work-function map, $\phi(x, y) = \phi_{\text{DFT}}(x, y) + \Delta\phi$, for the areas with CI greater than or equal to 0.1.

The roughness of the thermionic cathode used in this study is mainly due to machining and the grain structures. The range of the field-enhancement-factor values expected from the roughness features of typical thermionic cathodes is usually small, with an estimated upper bound of five [12,50,57,58]. Even in the case that the applied electric field is 500 V/mm, the difference in the Schottky-barrier lowering between a surface with a field-enhancement factor of $\beta = 5$ and a perfectly flat surface, $\beta = 1$, is only 0.033 eV, which will add a negligible enhancement to the thermionic emission, compared with the uncertainty of the DFT work-function values. Therefore, for simplicity in our model, we assume that the cathode surface is perfectly flat and neglect field-enhancement effects.

The grain orientations of areas with CI greater than or equal to 0.1 are considered as recognizable, and a work-function map $\phi(x, y) = \phi_{\text{DFT}}(x, y) + \Delta\phi$ is assigned to these areas. By choosing to assign a uniform reference value of zero to the cathode's Fermi energy, the boundary condition of Poisson's equation for each areas with CI greater than or equal to 0.1 is its vacuum level, $V(x, y, z = 0) = -\phi(x, y)/e$ [49]. Meanwhile, as the majority of pixels with CI less than 0.1 are associated with nonemitting areas, such as rough valleys, depressions, grain boundaries, and pores [53], we obtain the boundary conditions, $V(x, y, z = 0)$, for the cathode surface's areas with CI less than 0.1 by solving the two-dimensional (2D) Laplace's equation, $\nabla^2 V(x, y) = 0$. For the 2D boundary value at each edge of an area with CI less than 0.1, we use the V value of the adjacent areas with CI greater than or equal to 0.1. In this way, we obtain the boundary condition of the whole cathode surface, for both areas with CI greater than or equal to 0.1 and areas with CI less than 0.1, which is the input of the nonuniform emission model [49]. There is only one fitting parameter, $\Delta\phi$, in this model.

In the model, the potential energy for an electron present in the space within the diode is obtained by solving Poisson's equation, where the charge density is a nonlinear function of the potential energy in the space. The effect of Schottky-barrier lowering is included when calculating the potential energy. The patch-field effect is naturally included in the nonequipotential boundary condition at the cathode surface, $V(x, y, z = 0)$, and the 3D Poisson equation includes the 3D space-charge effect. Therefore, such a nonuniform emission model includes the effects of 3D space charge, patch fields, and Schottky-barrier lowering but neglects the effects of the lateral motion of electrons and the quantum effects (e.g., electron tunneling). More information on the physics and specific calculation methodology of our nonuniform emission model can be found in Ref. [49].

III. RESULTS AND DISCUSSION

A. Spatial distribution of work function

We use EBSD to characterize the spatial distribution of grain orientation for a particular cathode after emission testing is concluded on that cathode sample. We choose this ordering to ensure that our EBSD measurements capture any microstructural evolution that may occur during the high-temperature activation and emission-testing processes. Figure 3(a) shows the two-dimensional maps of grain orientation of a representative portion of a cathode

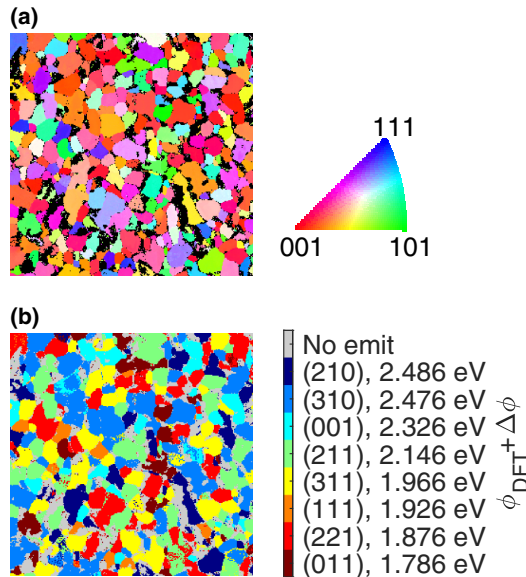


FIG. 3. (a) EBSD IPF of a commercial *S*-type cathode after cleanup. Areas where it is considered that grain orientations are unrecognized by EBSD are plotted in black. (b) Work-function map obtained by assigning the DFT work-function value [5] with a shift of $\Delta\phi = 0.176$ eV to the grain-orientation map (a) after grouping the orientations into one of the eight orientation groups.

surface (more details are given in Sec. III D). The percentage of each orientation group in the map is listed in Table I.

We measure the emitted current from a commercial *S*-type cathode made by 3M Technical Ceramics (Sec. II A) for various anode-cathode voltages and temperatures (Fig. 4). The anode-cathode distance, d , is obtained by fitting the FSCL data points using Eq. (2). In this work, we use 24 data points above 1340 K in Fig. 4(a) as the FSCL data points to obtain the anode-cathode distance, d , and the result is $d = 1.132$ mm. As expected, this is very close to the designed value of 1.06 mm. We ascribe the discrepancy between the fitted distance and the designed value to several reasonable factors, which include a likely small difference between the designed distance and actual fabricated distance (at room temperature) as well as the effects of electron optics and thermal expansion. The constant work-function shift is obtained by fitting all the data points in Fig. 4(a) with the nonuniform emission model, and the result is $\Delta\phi = 0.176$ eV, which indicates that DFT underestimates the work-function values compared with the thermionic emission-test results. This result is consistent with previous studies on the error of DFT-predicted work-function values [55,56] in terms of both the sign and magnitude of the error (underestimation by DFT of approximately 0.3 eV). Figure 3(b) is the predicted work-function map, which is obtained by applying shifted DFT work-function values to the grain-orientation map [Fig. 3(a)].

B. Emitted current density

Figure 4 shows experimental emission data from the *S*-type cathode (\times and $+$ symbols), the emitted current density predicted by applying the nonuniform emission model [49] (solid curves) to the work-function map [Fig. 3(b)], and the results predicted from a uniform cathode with a single work-function value (dotted curves).

The physics of nonuniform thermionic emission was not well studied before our work. It is conventional to use a single work-function value (a so-called “effective” work function) to describe the emission performance of a heterogeneous nonuniform thermionic cathode [59]. Scott [60] and Eng’s theoretical model [61] unifies the inclusion of the Schottky effect and space-charge effect, and therefore, is able to predict the TL, FSCL, and the TL-FSCL transition regions for a uniform cathode with a single work-function value in an infinite parallel diode. To investigate the consequence of applying their model, we assume that our *S*-type cathode sample can be described with a single work-function value, ϕ , and we obtain its value by fitting all the data points in Fig. 4(a) with Scott and Eng’s theoretical model. The result is $\phi = 2.021$ eV, which falls within the range of the local work-function values listed in Table I. Figure 4(a) shows that the approach

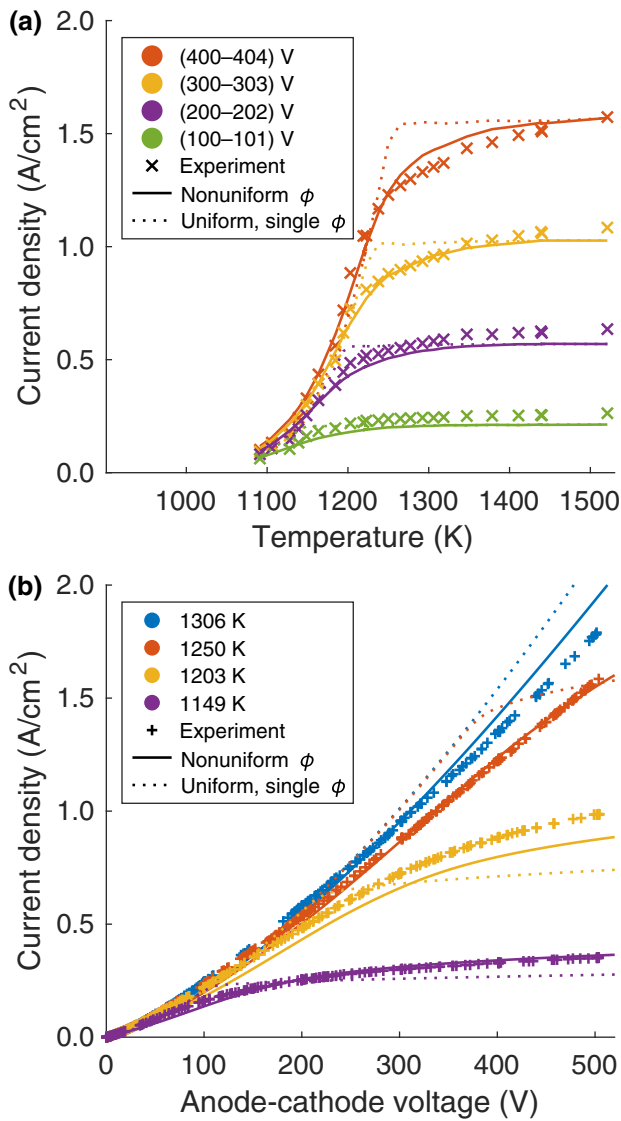


FIG. 4. Experimental data (\times and $+$ symbols) of an S -type cathode compared with the emitted current density predicted with the nonuniform emission model (solid curves), and the results predicted with a uniform cathode with a single fitted work-function value (dotted curves). (a) J - T curves for different anode-cathode voltages, V . Different colors denote different measured V values: red for data between 400 and 404 V, yellow for $300 \text{ V} \leq V \leq 303 \text{ V}$, purple for $200 \text{ V} \leq V \leq 202 \text{ V}$, and green for $100 \text{ V} \leq V \leq 101 \text{ V}$. (b) J - V curves, where different colors denote different temperatures.

of using a single effective work function can fit the TL and FSCL asymptotes in the J - T curves. However, this uniform cathode model is not able to accurately reproduce the smooth TL-FSCL transition from experimental observations. Figure 4(b) further reveals that such a single-work-function-value approach cannot predict the Schottky line (high-voltage asymptote in the J - V curves) observed in polycrystalline thermionic cathodes. Although the

uniform cathode model with a single work-function value is a simplified and well-studied model, it is not sufficient to predict some of the complex physical behavior present in the J - T and J - V curves from polycrystalline cathodes.

Such limitations of the uniform cathode model motivate our present work for developing a nonuniform emission model. For the same S -type cathode sample, Fig. 4 shows that our nonuniform emission model is in semi-quantitative agreement with experimental measurements, including predicted TL-FSCL transition regions that are as smooth as the experimental observations for both the J - T and J - V curves and predicted Schottky lines, which are in good agreement with the high- V asymptotes in the experimentally measured J - V curves. The gap between model and experimental results is significantly reduced by introducing the nonuniformity and relevant physical effects into the model.

There are only two fitting parameters in our model: the anode-cathode distance, $d = 1.132 \text{ mm}$, and the constant shift on DFT work-function values, $\Delta\phi = 0.176 \text{ eV}$. The main effect of a different d is to scale up and down the FSCL current, while the effect of a different $\Delta\phi$ is to scale up and down the TL current or shift the TL region to a lower or higher temperature in J - T curves. Using fitted values for these two parameters helps to get a better fit for the TL and FSCL regions, enabling a better comparison of the TL-FSCL transition regions between predicted curves and experimental results. The exact values of both of these fitted parameters have negligible effects on the shape of the TL-FSCL transition region (more details are given in the Supplemental Material [62]).

The smooth TL-FSCL transition in the predicted curves arises as a natural consequence of the nonuniform emission from the polycrystalline cathode with a nonuniform spatial distribution of the work function. Previous studies [39,40,47,48] show that the 3D space-charge effect plays a significant role in making the transition region smooth for a nonuniform cathode. However, when using a work-function map for a real cathode derived from DFT and EBSD, a model considering only the 3D space-charge effect predicts a TL-FSCL transition in a Miram curve sharper than the experimental results [47]. The nonuniform emission model used in this work [49] includes all of the effects of 3D space charge, patch fields, and Schottky-barrier lowering. This result shows that including all of these effects is required to predict the smooth TL-FSCL transition region in the J - T and J - V curves, not only for the checkerboard model cathode illustrated in Ref. [49], but also in a work-function map of a real cathode.

The Richardson constant, A , is an important factor in the Richardson-Laue-Dushman equation. Its theoretical value is $A = 4\pi mk_B^2 e/h^3 = 120.173 \text{ A cm}^{-2} \text{ K}^{-2}$. In multiple previous studies, the Richardson constant is experimentally obtained by fitting both the Richardson constant and the effective work function in the

Richardson-Laue-Dushman equation to experimental emission data under the assumption that the cathode is uniform and has a single work-function value [59]. It is observed that, using this method, the experimental values of the Richardson constant differ from the theoretical value, sometimes by many orders of magnitude [43,59]. However, the Richardson constant does not need to be fitted in our model and is assumed to be fixed to its theoretical value. Agreement between our experimental and predicted J - T and J - V curves indicates that alteration of the Richardson constant is not needed here. Thus, a key strength of our present model is that knowledge of the fractions of different surface terminations present, their arrangement in 2D space on the surface, and their work functions are all that is required for the nonuniform emission model to provide a physically complete picture of the emission.

C. Two-dimensional emission map

Figure 5 shows how the calculated emitted-current-density maps change as temperature increases and the emission changes from the TL region [Fig. 5(a)] to the transition region [Figs. 5(b) and 5(c)], and finally to the FSCL region [Fig. 5(d)]. To better illustrate the effects of the patch fields and space charge, we plot schematic figures of equipotential curves and electric flux lines in the space in front of a low-work-function patch surrounded by high-work-function patches in TL, transition, and FSCL regions (Fig. 6).

In the TL region [Fig. 5(a)], the space-charge effect is negligible, and therefore, the low-work-function patches emit more than the high-work-function patches. The result that the emitted current density varies across different grains due to the difference in work-function values (ϕ) is consistent with experimental ThEEM images obtained in the TL region [16,18–27].

As the schematic figures show, in the TL region [Fig. 6(a)], the space-charge effect is negligible, so the electrostatic potential in this case is close to the solution of the 3D Laplace equation, $\nabla^2 V(x, y, z) = 0$. The nonuniform boundary condition at the cathode surface, $V(x, y, z = 0) = -\phi(x, y)/e$, introduces additional electric fields between different work-function patches besides the applied electric field between the anode and the cathode. Therefore, equipotential contours and electric flux lines are bent in the space close to the patch boundaries. Such additional electric fields between different patches are referred to as the patch fields. The patch fields lead to a voltage minimum (potential depression, also called the virtual cathode) occurring a short distance above the edges of the strongly emitting low- ϕ patch. This causes the local emitted current density, $J(x, y)$, at the edge of low- ϕ patches to be smaller than the center of the patches [Fig. 5(a)] [46,63,64]. In the transition region [Fig. 5(b)], this patch-field effect continues to depress low-work-function patch

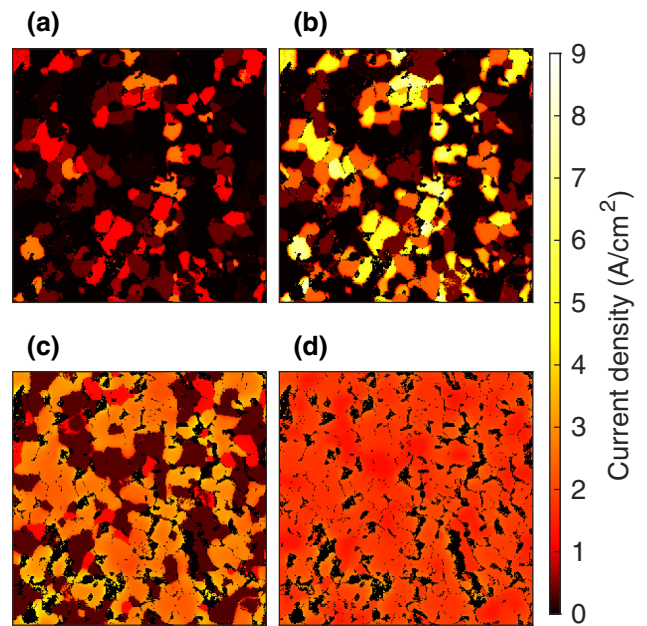


FIG. 5. Emitted-current-density maps, $J(x, y)$, predicted using the nonuniform emission model for a cathode with a work-function map as in Fig. 3(b) at anode-cathode voltage $V = 400$ V and distance $d = 1.132$ mm, at different temperatures: (a) TL region, temperature $T = 1149$ K; average emitted current density $J = 0.340$ A/cm²; (b) transition region, 1250 K; $J = 1.234$ A/cm²; (c) transition region but with an average emitted current density close to the FSCL value, 1411 K; $J = 1.525$ A/cm²; (d) FSCL region, 1521 K; $J = 1.552$ A/cm².

edge currents relative to their center currents, even though a potential depression begins to form above the patch center due to the space-charge effect [Fig. 6(b)]. Notably, the reduced edge emission of low-work-function patches due to patch fields contrasts with enhanced edge emission on a cathode surface with nonuniform emission but without patch-field effects. In the latter case, the edges of high-emitting patches emit more than the center of the patches due to the lower space charge in front of their neighboring low-emitting patches [36,37,40].

In the transition and FSCL regions [Figs. 6(b)–6(d)], the more-strongly-emitting low- ϕ patches have more significant space-charge effects than the less-emitting high- ϕ patches. As observed in Figs. 6(b) and 6(c), the strongly emitting low- ϕ patches develop voltage minima above their surfaces at these transition-region temperatures. This space-charge effect limits the emission from the low- ϕ patches, while the emission from the high- ϕ patches continues to increase without such limitation. This 3D space-charge effect causes the emission to become increasingly more spatially uniform as the temperature increases from the transition region to the FSCL region [Figs. 5(b)–5(d)].

In our nonuniform emission model, even though electrons are restricted along the cathode-anode direction with no lateral momentum, our model is able to predict the

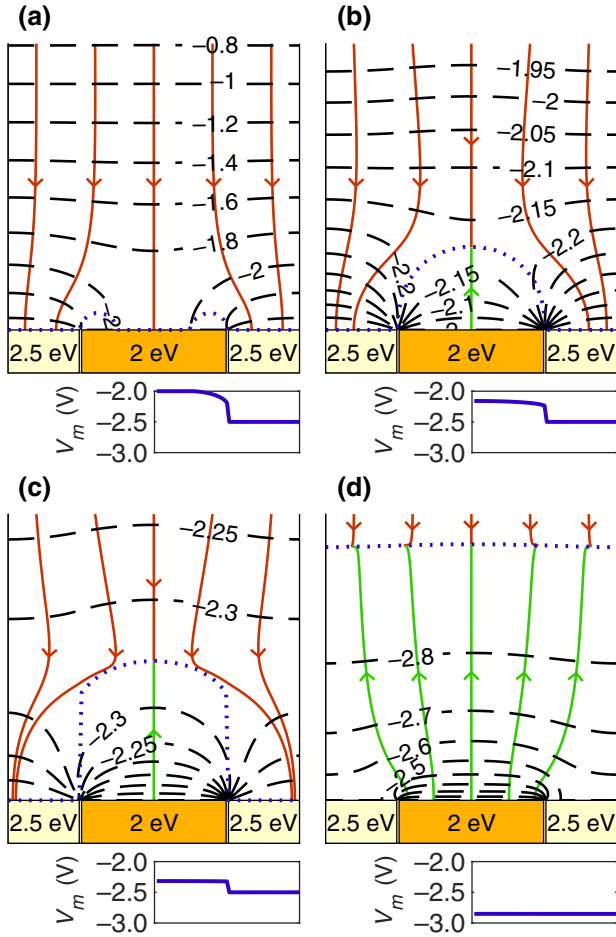


FIG. 6. Schematic figures illustrating the effects of patch fields and 3D space charge in different regions: (a) TL region, (b) transition region, (c) transition region with an average emitted current density close to FSCL value, and (d) FSCL region. Anode (not shown) is far away above the top of each subfigure, and the cathode is on the bottom of each subfigure, with a low-work-function patch (2 eV) surrounded by high-work-function patches (2.5 eV). Dashed black curves are equipotential contours of electrostatic potential (in V). Red and green solid curves are electric flux lines. Red ones are for electric flux lines starting from the anode, while green ones are for those starting from the cathode. Dotted violet curves indicate the position of voltage minimum, $z_m(x, y)$ (position of the virtual cathode). Plots beneath each subfigure (solid violet curves) show values of the voltage minimum in front of different locations of the cathode surface, $V_m(x, y)$. Value of $V_m(x, y)$ on the left half (not plotted) is symmetric to the right half. Local emitted current density is $J(x, y) = AT^2 \exp[-eV_m/(kT)]$.

trend of the change in the emission nonuniformity as temperature changes. Such a trend is also observed in experiments [65,66] and is consistent with some previous computational studies [39,40,47,48].

D. Sensitivity analysis and sources of error

It is computationally expensive to simulate large areas (for example, 0.1 mm² or larger) with the nonuniform

emission model and time-consuming to characterize the grain orientation of a large area where there are a large number of grains. The computational cost is significantly increased in beam-optics simulations, where millions of time steps are typically used [67]. To determine the representativeness of the statistics of the surface facets and ascertain the relationship between the uncertainty of the predicted emitted current and the size of the work-function map, we characterize a total of nine EBSD maps with sizes of 128 × 128 μm² on different regions of the S-type cathode, for a total examined area of 0.15 mm², and calculate the resulting emitted current density as a function of the examined area of the cathode surface.

To evaluate the effect of uncertainty in the work-function values to the predicted emitted current density, we calculate the emitted current density from a work-function map by applying $\phi(hkl) = \phi_{\text{DFT}}(hkl) + \Delta\phi(hkl)$ to the grain-orientation map in Fig. 3(a), where (hkl) is one of the eight grain orientations assigned with DFT work-function values, and the work-function shift for the eight grain orientations, $\Delta\phi(hkl)$, are assumed to be independent and identically distributed (IID) following the normal distribution, $\Delta\phi(hkl) \sim N(0.176 \text{ eV}, \sigma_{\text{DFT}}^2)$, where the standard deviation, σ_{DFT} , represents a phenomenological error in our DFT measurements. We generate 2500 random work-function maps for each σ_{DFT} value and calculate the variability of their emitted current densities.

Figure 7 shows the variability of the values of emitted current density for different submap sizes [Fig. 7(a)] and different uncertainties of work-function values [Fig. 7(b)] at a condition for the TL-FSCL transition region. Figure 7(a) shows how the prediction of emitted current density becomes more precise as the size of the submap increases, which indicates that model users may determine the submap size to use according to their desired precision in the prediction. Figure 7(b) estimates the uncertainty in the predicted emitted current density as a function of the uncertainty in the work-function values. Previous studies [55,56] estimate that the error of the DFT-predicted work-function values is on the scale of tenths of eV. Our results show that, even in the extreme case that the DFT work-function values have an uncertainty of 0.4 eV, the median [red line in the box in Fig. 7(b)] is 1.29 A/cm², close to 1.23 A/cm², which is the result for the baseline case [$\phi = \phi_{\text{DFT}} + 0.176 \text{ eV}$, Figs. 4 and 5(b)]. In the $\sigma_{\text{DFT}} = 0.4 \text{ eV}$ results, the first quartile (the lower edge of the box) is $Q_1 = 1.11 \text{ A/cm}^2$ while the third quartile (the upper edge) is $Q_3 = 1.41 \text{ A/cm}^2$, and the interquartile range (IQR) is $Q_3 - Q_1 = 0.29 \text{ A/cm}^2$. Such a dispersion is smaller than using a 32 × 32 μm² submap, which has an IQR of 0.37 A/cm², indicating a robustly predicted average current density, even for the higher end of DFT work-function uncertainty values.

Other possible causes of error in the predicted emitted current density include the measurement error in

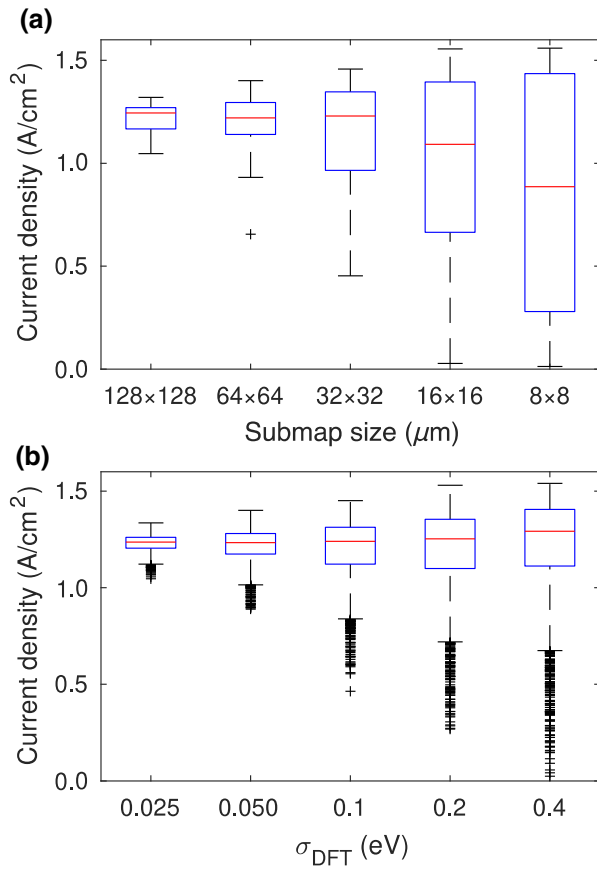


FIG. 7. Boxplots showing the variability of emitted current density predicted (a) from submaps of different characterized area sizes at temperature $T = 1250$ K, anode-cathode voltage $V = 400$ V, and distance $d = 1.132$ mm; (b) from a work-function map by applying $\phi(hkl) = \phi_{\text{DFT}}(hkl) + \Delta\phi(hkl)$ to the grain-orientation map in Fig. 3(a), where the shift values are IID following the normal distribution, $\Delta\phi(hkl) \sim N(0.176 \text{ eV}, \sigma_{\text{DFT}}^2)$. In a boxplot, the red line in the box indicates the median value. Lower edge of the box is the first quartile (Q_1 or 25th percentile). Upper edge is the third quartile (Q_3 or 75th percentile). Interquartile range (IQR) is defined as $Q_3 - Q_1$. Data points larger than $Q_3 + 1.5(Q_3 - Q_1)$ or smaller than $Q_1 - 1.5(Q_3 - Q_1)$ are considered as outliers and plotted individually using + symbols. Whiskers extend to the most-extreme data points not considered to be outliers.

temperature values, the dependence of the work-function value on temperature due to different stable arrangements of Ba-O surface species at different temperatures, and the dependence of the anode-cathode distance on temperature due to thermal expansion. The assumptions in the nonuniform emission model [49] may also contribute to the error in the predicted emission, which include the assumption of a perfectly flat cathode surface in an infinite parallel diode, neglecting lateral motion of the electrons, and neglecting quantum effects. While it is beyond the scope of the present work to perform an in-depth investigation of the role of each of these sources of error, we find it

very encouraging that the results in Fig. 4 illustrate that our model shows near-quantitative agreement with experiment over a wide range of temperatures and anode-cathode voltages. This strong agreement with experiment suggests that, while many sources of uncertainty in our model exist, they likely play a minor role in the resulting emission compared with the microstructural features of the cathode, including the fractions of each surface present, their size and spatial distribution, and the relative work functions of grains comprising the cathode surface.

IV. CONCLUSIONS AND OUTLOOK

Our nonuniform emission model can predict two-dimensional maps of emitted current density, and therefore, the average emitted current densities at different temperatures and anode-cathode voltages based on a two-dimensional work-function map derived by DFT calculations and microstructure characterization. Importantly, the predicted J - T and J - V curves are in semiquantitative agreement with experimental results, including the nature of the TL-FSCL transition, which shows the same shape as experiments. There are only two fitting parameters in our model: the anode-voltage distance and a constant shift of the DFT work-function values. The effect of these two fitting parameters on the shape of the TL-FSCL transition is negligible. Our model uses a physics-based modeling method coupled with experimental characterization to reproduce experimental emission data and illustrates that it is not necessary to use an empirical equation, such as the Longo-Vaughan equation, or to assume a continuous work-function distribution. A key result of this work is that a smooth TL-FSCL transition region is a natural consequence of the physics of the nonuniform emission from a spatial distribution work-function map when the effects of 3D space charge, patch fields, and Schottky-barrier lowering are included.

The present findings provide both a robust physics-based approach to predict the emitted current from any polycrystalline cathode for which the surface grain orientations and work functions are known, and a means to understand how the cathode microstructure and underlying work functions couple to the expected emission behavior. The present “forward” model starts from cathode work-function distributions and predicts J - T and J - V curves. In the future, it may be possible to create an “inverse” model, where one starts from experimentally measured J - T and/or J - V curves, and predict an effective cathode work-function arrangement and associated microstructure consistent with the measured emission. Such an approach may be an effective method to better understand the coupling of the cathode microstructure with the measured emission of new cathodes. Such a method would provide a powerful tool for understanding the expected emission behavior of new cathodes, as conducting an emission test on a new cathode

is less time-consuming than a full suite of microstructure and work-function studies, e.g., using EBSD characterization and DFT calculations. The results in this work can also be used as inputs for higher-level simulation codes like MICHELLE [67] to improve the modeling of cathodes in electron-gun fixtures, better informing device design and enabling a deeper insight into the physical factors governing heterogeneous emission from thermionic cathodes.

Raw data of the figures are available in the Supplemental Material [62]. Codes for the nonuniform emission model are available on GitHub [68].

ACKNOWLEDGMENTS

This work is funded by the Defense Advanced Research Projects Agency (DARPA) through the Innovative Vacuum Electronic Science and Technology (INVEST) program with Leidos, Inc. The authors would like to thank Daniel Busbaher from 3M Technical Ceramics for providing the cathodes from which the data are obtained. The authors gratefully acknowledge use of facilities and instrumentation supported by NSF through the University of Wisconsin Materials Research Science and Engineering Center (Grant No. DMR-1720415).

-
- [1] D. M. Kirkwood, S. J. Gross, T. J. Balk, M. J. Beck, J. Booske, D. Busbaher, R. Jacobs, M. E. Kordesch, B. Mitsdarffer, D. Morgan, *et al.*, Frontiers in thermionic cathode research, *IEEE Trans. Electron Devices* **65**, 2061 (2018).
- [2] J. Cronin, Modern dispenser cathodes, *IEE Proc., Part I: Solid-State Electron Devices* **128**, 19 (1981).
- [3] V. Vlahos, Y.-L. Lee, J. H. Booske, D. Morgan, L. Turek, M. Kirshner, R. Kowalczyk, and C. Wilsen, *Ab initio* investigation of the surface properties of dispenser *B*-type and scandate thermionic emission cathodes, *Appl. Phys. Lett.* **94**, 184102 (2009).
- [4] A. Gilmour, *Klystrons, TWTs, Magnetrons, Crossed-Field Amplifiers, and Gyrotrons* (Artech House, Boston, MA, 2011).
- [5] R. Jacobs, D. Morgan, and J. Booske, Work function and surface stability of tungsten-based thermionic electron emission cathodes, *APL Mater.* **5**, 116105 (2017).
- [6] Q. Zhou, X. Liu, T. Maxwell, B. Vancil, T. J. Balk, and M. J. Beck, $\text{Ba}_x\text{Sc}_y\text{O}_z$ on W (001), (110), and (112) in scandate cathodes: Connecting to experiment via μ_0 and equilibrium crystal shape, *Appl. Surf. Sci.* **458**, 827 (2018).
- [7] X. Liu, Q. Zhou, T. L. Maxwell, B. K. Vancil, M. J. Beck, and T. J. Balk, Scandate cathode surface characterization: Emission testing, elemental analysis and morphological evaluation, *Mater. Charact.* **148**, 188 (2019).
- [8] J. Wang, Y. Yang, Y. Wang, W. Liu, M. Zhou, and T. Zuo, A review on scandia doped tungsten matrix scandate cathode, *Tungsten* **1**, 91 (2019).
- [9] R. J. Barker, N. C. Luhmann, J. H. Booske, and G. S. Nusinovich, *Modern Microwave and Millimeter-Wave Power Electronics* (Wiley-IEEE Press, Piscataway, NJ, 2005).
- [10] J. H. Booske, Plasma physics and related challenges of millimeter-wave-to-terahertz and high power microwave generation, *Phys. Plasmas* **15**, 055502 (2008).
- [11] D. Jones, D. McNeely, and L. W. Swanson, Surface and emission characterization of the impregnated dispenser cathode, *Appl. Surf. Sci.* **2**, 232 (1979).
- [12] K. L. Jensen, D. W. Feldman, M. Virgo, and P. G. O'Shea, Measurement and analysis of thermal photoemission from a dispenser cathode, *Phys. Rev. Spec. Top. - Accel. Beams* **6**, 083501 (2003).
- [13] Y. Wan, Y. Li, Q. Wang, K. Zhang, and Y. Wu, The relationship of surface roughness and work function of pure silver by numerical modeling, *Int. J. Electrochem. Sci.* **7**, 5204 (2012).
- [14] R. Forman, Surface studies of barium and barium oxide on tungsten and its application to understanding the mechanism of operation of an impregnated tungsten cathode, *J. Appl. Phys.* **47**, 5272 (1976).
- [15] G. A. Haas, A. Shih, and C. R. K. Marrian, Interatomic Auger analysis of the oxidation of thin Ba films, *Appl. Surf. Sci.* **16**, 139 (1983).
- [16] D. Norman, R. A. Tuck, H. B. Skinner, P. J. Wadsworth, T. M. Gardiner, I. W. Owen, C. H. Richardson, and G. Thornton, Surface Structure of Thermionic-Emission Cathodes, *Phys. Rev. Lett.* **58**, 519 (1987).
- [17] V. Vlahos, J. H. Booske, and D. Morgan, *Ab initio* investigation of barium-scandium-oxygen coatings on tungsten for electron emitting cathodes, *Phys. Rev. B* **81**, 054207 (2010).
- [18] G. A. Haas and R. E. Thomas, Work-function distribution studies of pressed matrix cathodes, *J. Appl. Phys.* **38**, 3969 (1967).
- [19] M. V. Mroz, T. Savina, M. E. Kordesch, J. T. Sadowski, and S. A. Tenney, Solid-solid dewetting of scandium thin films on the W(100) surface observed using emission microscopy, *J. Vac. Sci. Technol., B* **37**, 012903 (2019).
- [20] R. A. Tuck, Surface studies of thermionic emitters by methods unique to them, *Appl. Surf. Sci.* **2**, 128 (1979).
- [21] C. Wan, J. M. Vaughn, J. T. Sadowski, and M. E. Kordesch, Scandium oxide coated polycrystalline tungsten studied using emission microscopy and photoelectron spectroscopy, *Ultramicroscopy* **119**, 106 (2012).
- [22] J. M. Vaughn, K. D. Jamison, and M. E. Kordesch, *In situ* emission microscopy of scandium/scandium-oxide and barium/barium-oxide thin films on tungsten, *IEEE Trans. Electron Devices* **56**, 794 (2009).
- [23] J. M. Vaughn, K. D. Jamison, and M. E. Kordesch, in *2010 IEEE International Vacuum Electronics Conference (IVEC)* (IEEE, 2010), pp. 421–422.
- [24] M. E. Kordesch and C. Wan, in *2013 26th International Vacuum Nanoelectronics Conference (IVNC)* (IEEE, 2013), pp. 1–2.
- [25] C. Wan and M. E. Kordesch, Tungstate formation in a model scandate thermionic cathode, *J. Vac. Sci. Technol., B: Nanotechnol. Microelectron.: Mater., Process., Meas., Phenom.* **31**, 011210 (2013).
- [26] F. Ren, S.-Y. Yin, Z.-P. Lu, Y. Li, Y. Wang, S.-J. Zhang, F. Yang, and D. Wei, Applications of deep ultraviolet laser photo- and thermal-emission electron microscope in thermal dispenser cathode research, *Acta Phys. Sin.* **66**, 187901 (2017).

- [27] M. Mroz, S. Tenney, T. Savina, and M. E. Kordesch, Thermionic emission microscopy of scandium thin film dewetting on W(100), *AIP Adv.* **8**, 065114 (2018).
- [28] O. W. Richardson, The emission of electricity from hot bodies, *J. Röntgen Soc.* **18**, 150 (1922).
- [29] S. Dushman, Thermionic emission, *Rev. Mod. Phys.* **2**, 381 (1930).
- [30] W. Schottky, Über kalte und warme Elektronenentladungen, *Zeitschrift Für Phys.* **14**, 63 (1923).
- [31] C. D. Child, Discharge from hot CaO, *Phys. Rev. (Series I)* **32**, 492 (1911).
- [32] I. Langmuir, The effect of space charge and initial velocities on the potential distribution and thermionic current between parallel plane electrodes, *Phys. Rev.* **21**, 419 (1923).
- [33] T. C. Fry, The thermionic current between parallel plane electrodes; velocities of emission distributed according to Maxwell's law, *Phys. Rev.* **17**, 441 (1921).
- [34] J. W. Luginsland, Y. Y. Lau, and R. M. Gilgenbach, Two-Dimensional Child-Langmuir Law, *Phys. Rev. Lett.* **77**, 4668 (1996).
- [35] Y. Y. Lau, Simple Theory for the Two-Dimensional Child-Langmuir Law, *Phys. Rev. Lett.* **87**, 278301 (2001).
- [36] R. J. Umstadtd and J. W. Luginsland, Two-Dimensional Space-Charge-Limited Emission: Beam-Edge Characteristics and Applications, *Phys. Rev. Lett.* **87**, 145002 (2001).
- [37] J. W. Luginsland, Y. Y. Lau, R. J. Umstadtd, and J. J. Watrous, Beyond the Child-Langmuir law: A review of recent results on multidimensional space-charge-limited flow, *Phys. Plasmas* **9**, 2371 (2002).
- [38] Y.-M. QUAN and Y.-G. DING, Generalization of the two-dimensional Child-Langmuir law for non-zero injection velocities in a planar diode, *J. Plasma Phys.* **75**, 85 (2009).
- [39] A. Sitek, K. Torfason, A. Manolescu, and Á Valfells, Space-Charge Effects in the Field-Assisted Thermionic Emission from Nonuniform Cathodes, *Phys. Rev. Appl.* **15**, 014040 (2021).
- [40] A. Sitek, K. Torfason, A. Manolescu, and Á Valfells, Edge Effect on the Current-Temperature Characteristic of Finite-Area Thermionic Cathodes, *Phys. Rev. Appl.* **16**, 034043 (2021).
- [41] R. T. Longo, in *1980 International Electron Devices Meeting* (IRE, 1980), pp. 467–470.
- [42] R. Vaughan, A synthesis of the Longo and Eng cathode emission models, *IEEE Trans. Electron Devices* **33**, 1925 (1986).
- [43] A. S. Gilmour, *Principles of Traveling Wave Tubes* (Artech House, Norwood, MA, 1994).
- [44] J. C. Tonnerre, D. Brion, P. Palluel, and A. M. Shroff, Evaluation of the work function distribution of impregnated cathodes, *Appl. Surf. Sci.* **16**, 238 (1983).
- [45] M. Cattelino and G. Miram, Predicting cathode life expectancy and emission quality from PWFd measurements, *Appl. Surf. Sci.* **111**, 90 (1997).
- [46] L. K. Hansen, Anomalous Schottky effect, *J. Appl. Phys.* **37**, 4498 (1966).
- [47] D. Chernin, Y. Y. Lau, J. J. Petillo, S. Ovtchinnikov, D. Chen, A. Jassem, R. Jacobs, D. Morgan, and J. H. Booske, Effect of nonuniform emission on Miram curves, *IEEE Trans. Plasma Sci.* **48**, 146 (2020).
- [48] A. Jassem, D. Chernin, J. J. Petillo, Y. Y. Lau, A. Jensen, and S. Ovtchinnikov, Analysis of anode current from a thermionic cathode with a 2-D work function distribution, *IEEE Trans. Plasma Sci.* **1**, 749 (2021).
- [49] D. Chen, R. Jacobs, D. Morgan, and J. Booske, Impact of nonuniform thermionic emission on the transition behavior between temperature-and space-charge-limited emission, *IEEE Trans. Electron Devices* **68**, 3576 (2021).
- [50] K. L. Jensen, Y. Y. Lau, and N. Jordan, Emission nonuniformity due to profilometry variation in thermionic cathodes, *Appl. Phys. Lett.* **88**, 164105 (2006).
- [51] D. P. Field, Recent advances in the application of orientation imaging, *Ultramicroscopy* **67**, 1 (1997).
- [52] M. M. Nowell and S. I. Wright, Orientation effects on indexing of electron backscatter diffraction patterns, *Ultramicroscopy* **103**, 41 (2005).
- [53] S. I. Wright and M. M. Nowell, EBSD image quality mapping, *Microsc. Microanal.* **12**, 72 (2006).
- [54] D. Chen, R. Jacobs, V. Vlahos, D. Morvan, and J. Booske, in *2019 International Vacuum Electronics Conference (IVEC)* (IEEE, 2019), pp. 1–2.
- [55] S. De Waele, K. Lejaeghere, M. Sluydts, and S. Cottenier, Error estimates for density-functional theory predictions of surface energy and work function, *Phys. Rev. B* **94**, 235418 (2016).
- [56] R. Tran, X.-G. Li, J. H. Montoya, D. Winston, K. A. Persson, and S. P. Ong, Anisotropic work function of elemental crystals, *Surf. Sci.* **687**, 48 (2019).
- [57] R. Miller, Y. Y. Lau, and J. H. Booske, Electric field distribution on knife-edge field emitters, *Appl. Phys. Lett.* **91**, 1 (2007).
- [58] R. Miller, Y. Y. Lau, and J. H. Booske, Schottky's conjecture on multiplication of field enhancement factors, *J. Appl. Phys.* **106**, 104903 (2009).
- [59] V. S. Fomenko, *Handbook of Thermionic Properties* (Springer US, Boston, MA, 1966).
- [60] J. B. Scott, Extension of Langmuir space-charge theory into the accelerating field range, *J. Appl. Phys.* **52**, 4406 (1981).
- [61] G. Eng, A new correction to Schottky barrier lowering in cathodes, *J. Appl. Phys.* **58**, 4365 (1985).
- [62] See the Supplemental Material at <http://link.aps.org/supplemental/10.1103/PhysRevApplied.18.054010> for a more detailed discussion of the fitted values of work function and anode-cathode distance and raw data of the figures.
- [63] J. A. Becker, Thermionic electron emission and adsorption part I. Thermionic emission, *Rev. Mod. Phys.* **7**, 95 (1935).
- [64] C. Herring and M. H. Nichols, Thermionic emission, *Rev. Mod. Phys.* **21**, 185 (1949).
- [65] J. Li, H. Wang, Y. Gao, H. Yuan, K. Pan, K. Zhang, Q. Chen, T. Yan, F. Liao, J. Wang, Y. Wang, and W. Liu, in *2006 IEEE International Vacuum Electronics Conference Held Jointly with 2006 IEEE International Vacuum Electron Sources* (IEEE, 2006), pp. 51–52.
- [66] J. Li, H. Wang, Z. Yu, Y. Gao, Q. Chen, and K. Zhang, in *2007 IEEE International Vacuum Electronics Conference* (IEEE (2007), Vol. 2440, pp. 1–2.
- [67] J. Petillo, K. Eppley, D. Panagos, P. Blanchard, E. Nelson, N. Dionne, J. DeFord, B. Held, L. Chernyakova, W. Krueger, S. Humphries, T. McClure, A. Mondelli, J. Burdette, M. Cattelino, R. True, K. T. Nguyen, and B. Levush, The Michelle three-dimensional electron gun and collector modeling tool: Theory and design, *IEEE Trans. Plasma Sci.* **30**, 1238 (2002).
- [68] <https://github.com/chen-dongzheng/nonuniform-emission>